IEEE Access
Multidisciplinary ⋮ Rapid Review ⋮ Open Access Journal

Received 26 November 2022, accepted 5 December 2022, date of publication 12 December 2022,
date of current version 16 December 2022.

Digital Object Identifier 10.1109/ACCESS.2022.3228273

RESEARCH ARTICLE

Frequency Characteristics of the Synchronous Motor-Generator Pair to Elevate the Upper Limit Penetration Rate of Renewable Energy Sources

GUOJIAN LI[1], ERFA SHANG[2], QIANYU WU[3], (Student Member, IEEE), CHENYANG LI[4], (Graduate Student Member, IEEE), AND JINPING KANG[4], (Member, IEEE)

[1]SPIC Inner Mongolia Energy Company Ltd., Tongliao, Inner Mongolia 028000, China
[2]Inner Mongolia Xilin Gol League Dian Tou New Energy Company Ltd., Xilinhaote, Inner Mongolia 026000, China
[3]North China Branch of State Grid Corporation of China, Beijing 100053, China
[4]State Key Laboratory of Alternate Electrical Power System With Renewable Energy Sources, North China Electric Power University, Beijing 102206, China

Corresponding author: Chenyang Li (lichenyang1996@qq.com)

This work was supported in part by the Independent Research Project of State Key Laboratory of Alternate Electrical Power System with Renewable Energy Sources under Grant LAPS202202.

ABSTRACT With the increase of renewable energy sources (RES) in power systems, the number of traditional synchronous generators (SGs) declines gradually, which leads to a decrease in total inertia and frequency instability in extreme situations. The synchronous motor-generator pair (MGP) system was proposed as a new grid-connection method to improve the inertial response and frequency stability of grids. To study the effects of the MGP on the frequency stability and penetration rate of RES in power grids, first the frequency response equations of a single MGP in a single-machine infinite bus system are derived; then, the system frequency response (SFR) model for a multi-machine system with the MGP integrated is built. By comparing key critical indices of the frequency response after step disturbance with this model, we discover that the MGP system can increase the upper limit penetration rate of RES by quite a percentage. Furthermore, time domain simulations are used to compare the frequency characteristics of RES penetration rates of 25%, 50% and 75% with and without MGP. Finally, the MGP test bench is built for relevant experimental verification.

INDEX TERMS Renewable energy sources (RES), motor-generator pair (MGP), inertial response, dynamic frequency response characteristics, upper limit penetration rate of RES.

NOMENCLATURE

A. ACRONYMS

RES	Renewable energy sources
SG	Synchronous generator
MGP	Motor-generator pair
SFR	System frequency response
DFIGs	Doubly-fed induction generators
PMSGs	Permanent magnet synchronous generators
PV	Photovoltaic
VSG	Virtual synchronous generator
SM	Synchronous motor
HVRT	High voltage ride through
LVRT	Low voltage ride through
EMF	Electromotive force
RoCoF	Rate of change of frequency

B. VARIABLES

J	Moment of inertia
r	Radius of rotation
m	Mass of rigid body
H	Inertia constant
ω_0	Synchronous speed
S_B	Rated capacity
H_C	Inertial constant of PV capacitor
C	Capacitance of DC side of the inverter
U_C	Capacitor voltage
S_N	Rated installed capacity of renewable energy

The associate editor coordinating the review of this manuscript and approving it for publication was Junjian Qi.

E'_{M}	Induced EMF in stator windings of the SM
E'_{G}	Induced EMF in stator windings of the SG
U_{BM}	Terminal voltage of the SM
U_{BG}	Terminal voltage of the SG
I_{M}	Stator current of the SM
I_{G}	Stator current of the SG
x'_{dM}	Direct-axis transient reactance of the SM
x'_{dG}	Direct-axis transient reactance of the SG
δ_{M}	Power angle of the SM
δ_{G}	Power angle of the SG
ΔP_{MGP}	Deviation power of the MGP
ΔP_{M}	Deviation power of the SM
ΔP_{G}	Deviation power of the SG
$\Delta\delta_{\mathrm{M}}$	Deviation of power angle of the SM
$\Delta\delta_{\mathrm{G}}$	Deviation of power angle of the SG
$\Delta\delta_{\mathrm{MG}}$	Deviation of power angle of the MGP
T_{eM}	Input torque of the MGP
T_{eG}	Output torque of the MGP
K_{sM}	Synchronous torque coefficient of the SM
K_{sG}	Synchronous torque coefficient of the SG
T_{mM}	Mechanical torque of the SM
T_{mG}	Mechanical torque of the SG
ω_{M}	Rotor speed of the SM
ω_{G}	Rotor speed of the SG
ω_{MGP}	Rotor speed of the MGP
H_{MGP}	Inertial constant of MGP
$\Delta\omega_{\mathrm{M}}$	Deviation of rotor speed of the SM
$\Delta\omega_{\mathrm{G}}$	Deviation of rotor speed of the SG
$\Delta\omega_{\mathrm{MGP}}$	Deviation of rotor speed of the MGP
ΔT_{eM}	Deviation of electromagnetic torque of the SM
ΔT_{eG}	Deviation of electromagnetic torque of the SG
K_{DM}	Damping coefficient of the SM
K_{DG}	Damping coefficient of the SG
$\Delta\omega_{\mathrm{r}}$	Frequency deviation of power system
H_{G}	Inertial constant of traditional generator unit
D	Damping factor
R	Governor regulator coefficient
T_{R}	Reheater time constant
F_{H}	Fraction of total power generated by the high-pressure turbine
ΔP_{L}	Deviation of the load power
ΔP_{m}	Mechanical power deviation of generator units
ΔP_{e}	Electromagnetic power deviation of generator units
ω_{n}	Natural oscillation frequency
ζ	Damping ratio
ω_{fr}	Damped frequency
t_{nadir}	Time corresponding to the maximum frequency deviation
$\Delta f_{\mathrm{ssMGP}}$	Steady-state deviation of frequency response for power systems with MGP
$\Delta f_{\mathrm{nadirMGP}}$	Maximum frequency deviation for power systems with MGP
$\Delta f_{\mathrm{ssnew}}$	Steady-state deviation of frequency response for power systems without MGP
$\Delta f_{\mathrm{nadirnew}}$	Maximum frequency deviation for power systems without MGP

I. INTRODUCTION

Due to insufficient system inertia and primary frequency regulation, a large-scale power outage occurred in the United Kingdom on August 9, 2019, with a loss of approximately 3.2% of the load [1]. The maximum power point tracking curve is widely used to extract the maximum energy from variable renewable energy sources (RES). The output electromagnetic powers of RES, including doubly-fed induction generators (DFIGs), permanent magnet synchronous generators (PMSGs) and photovoltaic (PV), cannot allocate disturbance power automatically. There is no bearing of RES extraction with respect to frequency changes of the system [2]. In the power system with high penetration of RES, where a large number of traditional synchronous generators (SGs) are replaced, the moment of inertia is relatively reduced, which speeds up the frequency deviation under disturbance. In addition, the low tolerance of disturbance of RES may further increase unbalanced powers and seriously deteriorate the frequency stability of the grids.

In order to improve the inertial response, most of the previous studies controlled the converters to improve the frequency adjustment capabilities. To achieve the virtual inertial response, an additional control link for active power control of wind turbines was added in [3]. By optimizing the short-term overproduction response of variable-speed wind turbines, the synthetic inertia provision was realized in [4]. Additionally, frequency-droop control imitated the self-regulation capability of SGs to control the power regulation of RES [5]. The droop control through active power was presented in [6] for the primary frequency regulation of RES. Virtual inertia control and droop control were combined to improve the response characteristics of wind turbines to frequency changes of systems in [7] and [8]. The deviation and rate of change of frequency were introduced into the active power control loop of wind turbines to realize the comprehensive inertia control [9]. To mimic the inertial response and damping characteristics of SGs, virtual synchronous generator (VSG) technology was proposed in [10], [11], and [12]. Working with about 10% output margin, the load reduction scheme of wind turbines proposed in [13] can provide inertia response and primary frequency regulation, whereas the scheme cannot work when the output of wind farms is low [14].

However, the existing methods through control of inverters to improve frequency stability have certain limitations. For instance, the inertial response from the kinetic energy of wind turbine's rotor can be of short duration and cause the second frequency drop. Because of the constraints of the extreme values for the rotor speed of wind turbines, the adjustment ability is limited. Besides, the setting of control parameters

is complicated and subject to external influence. How to set the control parameters scientifically and accurately is still challenging in practice. In addition, the remaining SGs have to share more disturbance power with some SGs replaced by RES, and this leads to an increase in the rate of change of frequency. Because of the current source characteristics of virtual inertia and droop control [15], RES cannot able to instantaneously allocate disturbance power according to the synchronous power coefficient in such a control mode [16]. Theoretically, VSG technology can share power disturbance instantaneously, but the large instantaneous unbalanced torque affects the stable operation of RES and there are still control delays in the VSG control.

In contrast, traditional SGs can distribute the disturbance power instantaneously according to their synchronizing power coefficients [17]. Besides, the rotating rotors have reliable inertial response and can respond to the power deviation of the system to support the power balance and restrains the frequency deviation [18], [19]. Therefore, based on the theory of SGs, the MGP was proposed as a possible grid-connection approach to improve the stability of high proportion RES systems [20]. Based on this idea, first the oscillation mode was studied and compared through its small signal model, which demonstrated the improvements of MGP on stability region and damping ratio over traditional grid-connected inverters [21], [22], and then time domain simulation results during the faults verified that MGP can effectively improve the transient stability of grids [23]. In addition, the fault isolation capability of RES can be enhanced significantly by MGP [24]. Though the frequency stability improvement were studied in different scenarios, the effects of the MGP on the critical penetration rate of RES and quantitative calculations have not been investigated. Thus, How the integration of MGP affects the penetration rate of RES deserves further study.

To fulfill this gap and as a part of the continuous research, the main goal of this study is to illustrate the role of MGP system in stability enhancement with different penetration of RES in multi-machine systems and try to find their critical penetration rate. This paper is organized as follows. Section II presents the operating principle of MGP. In Section III, the frequency response of a single MGP is derived for a single-machine infinite bus system. In Section IV, the system frequency response (SFR) model of a multi-machine system whose RES is connected to grids via MGP is proposed according to its transfer functions. In addition, a relationship is established between the key indices for time domain frequency stability and the proportion rate of RES with MGP. The upper-limit penetration rate of RES is then calculated, and time-domain analysis on the frequency response of multi-machine systems is also carried out. In Section V, a single MGP experimental setup and multi-machine experimental bench, including PV and MGP, are established to validate the enhanced influence of MGP on the frequency response.

II. CONCEPTUAL STUDY OF THE MGP

A. STRUCTURE OF THE MGP

Fig.1 illustrates the layout of MGP and its application scheme. The MGP consists of an SM and SG, where their rotors are connected to the same mechanical shaft. The electricity generated by RES is used to drive the SM to convert electrical energy into mechanical energy. The SM drives the SG through a mechanical shaft, and the SG converts mechanical energy into electrical energy. Two machines rotate at the same speed on steady state. The excitation systems and control system adjust the power transmitted by the MGP system.

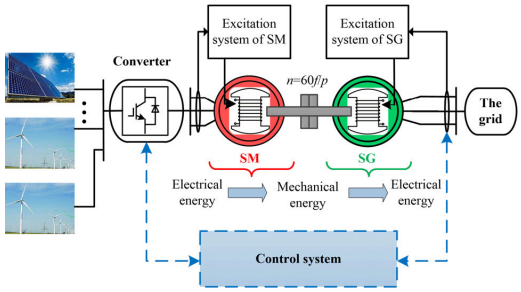

FIGURE 1. The structure and layout of MGP.

The useful features of the MGP system can be easily predicted based on its structure. For example, it has real inertia, it electrically isolates the RES and the grid, it can withstand overvoltage and overcurrent, it provides reactive power support to the grid, etc. However, the power consumption of rotation machines and additional investment cost may limit the application of MGP at low level penetration RES. Based on a 5.5 kW MGP experimental test bench, the measured efficiency is 91.7%. With the expansion of capacity, the efficiency of the whole system is significantly improved. The additional costs of MGP mainly include the costs of two SGs, a converter, installation, and civil engineering. MGP can provide sufficient reactive power support and realize high voltage ride through (HVRT) and low voltage ride through (LVRT) [24], [25]. Reactive power compensation devices and converter modification of HVRT and LVRT for RES stations can be avoided. Besides, as more and more existing conventional units are replaced by RES, the potential costs of machines will be reduced if decommissioned thermal units can be reused.

From a systematic point of view, the MGP can increase the stability of the grid at the RES ends, where the strength is usually weak. Hopefully, the MGP may be one of the most effective grid-connection methods for the future grid with an ultra-high proportion of RES [26].

B. INERTIA OF MGP

The MGP system can increase inertial response of power grids. The inertia of a power system is a resistance to frequency deviation caused by external disturbances.

The moment of inertia J is a physical quantity that characterizes the rotational inertia of a rigid body, which can be estimated with the mass block as in (1).

$$J = \int r^2 dm \tag{1}$$

Based on the mass parameters of a thermal generator, the moment of inertia of an MGP with the same capacity is estimated. For a conventional thermal power generator, the rotational part is composed of the exciter, SG, low-pressure cylinder, and high-pressure cylinder. The MGP system consists of two synchronous machines and two sets of excitation systems. Thus, the moment of inertia of the MGP is about 65% that of a thermal generator with the same capacity, as shown in Appendix A [27].

The moment of inertia J can be expressed by the inertia constant H, as shown in (2).

$$H = \frac{1}{2}\frac{J\omega_0^2}{S_B} \tag{2}$$

For example, suppose that the inertia constant H of a 600MW turbogenerator is 6.636s. Then, similarly, H of a MGP with the same capacity can be calculated as 4.38s.

The virtual inertia of PV is entirely derived from the energy storage of the capacitor on the DC side of the inverter. The inertial constant of PV capacitor H_C is in (3).

$$H_C = \frac{1}{2}\frac{CU_C^2}{S_N} \tag{3}$$

Taking U_C as 625V and C as 0.1F in (3), the inertial constant H_C of 600MW PV can be calculated as 0.01659s. Therefore, the inertia of the MGP is about 400 times that of an inverter with the same capacity.

C. POWER ANGLE CHARACTERISTICS OF MGP

An equivalent electrical circuit with the classical model for MGP is shown in Fig.2. The shafts of the two machines of the MGP are coupled, therefore, the angular speeds of two machines rotors are the same if the torsional stiffness of the shafts is ignored. Then, E'_M and E'_G rotate synchronously at the synchronous speed ω_0.

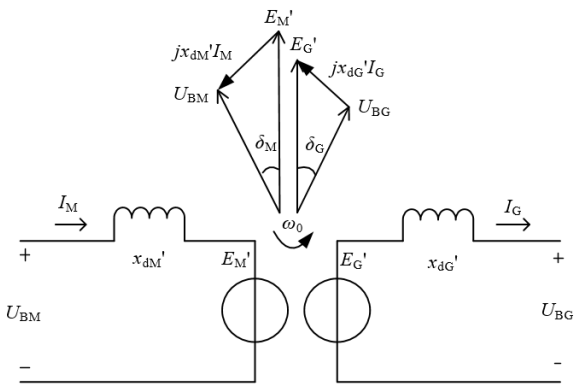

FIGURE 2. Equivalent electrical circuit with the classical model for MGP.

Ignoring the loss of MGP, the deviation power of MGP, ΔP_{MGP}, the deviation power of SM, ΔP_M, and the deviation power of SG, ΔP_G, interact with one another. ΔP_M and ΔP_G can be expressed as (4) and (5).

$$\Delta P_M = \frac{|U_{BM}|\,|E'_M|}{x'_{dM}}\cos\delta_{M0}\Delta\delta_M \tag{4}$$

$$\Delta P_G = \frac{|U_{BG}|\,|E'_G|}{x'_{dG}}\cos\delta_{G0}\Delta\delta_G \tag{5}$$

According to (4) and (5), ΔP_M and ΔP_G have the same changing trend as $\Delta\delta_M$and $\Delta\delta_G$. To measure the phase disturbance of MGP when the power fluctuates, we define the deviation of power angle of MGP, $\Delta\delta_{MG}$, as shown in (6) and Fig.3. In dynamic disturbance analysis, $\Delta\delta_{MG}$ can be used as the state variable to measure the power angle change of MGP.

$$\Delta\delta_{MG} = \Delta\delta_M + \Delta\delta_G \tag{6}$$

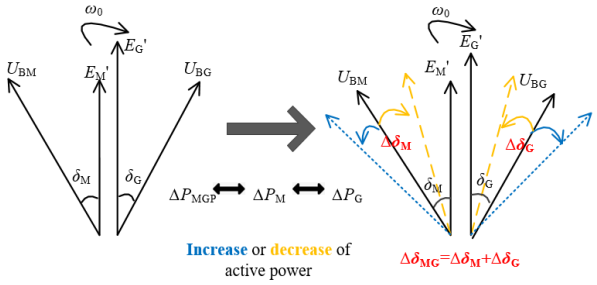

FIGURE 3. Power angle characteristic of MGP.

III. FREQUENCY RESPONSE CHARACTERISTIC OF A SINGLE MGP

A. CLASSIC SECOND-ORDER MATHEMATICAL MODEL OF MGP

Fig.4 illustrates the scheme of a MGP connected to an infinite bus.

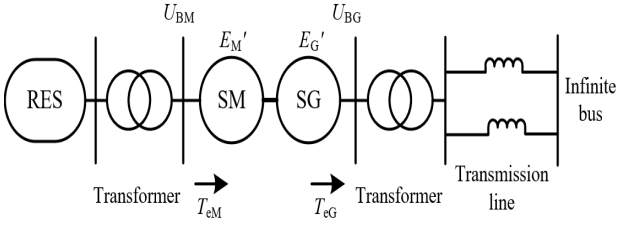

FIGURE 4. Equivalent circuit of a single-machine infinite bus system with MGP.

In a single-machine infinite bus system with MGP shown in Fig.4, the input torque T_{eM} and output torque T_{eG} of the MGP are linearized and can be described as (7), and (8).

$$\Delta T_{eM} = K_{sM}\Delta\delta_M = \frac{|E'_M|\,|U_{BM}|}{x'_{dM}}\cos\delta_{M0}\Delta\delta_M \tag{7}$$

$$\Delta T_{eG} = K_{sG}\Delta\delta_G = \frac{|E'_G|\,|U_{BG}|}{x'_{dG}}\cos\delta_{G0}\Delta\delta_G \tag{8}$$

Considering the MGP as a whole mass block, the SM's mechanical torque T_{mM} and the angular speed ω_M are equal to the SG's mechanical torque T_{mG} and the angular speed ω_G, respectively. The inertia constants H of two machines are equal. The inertial constant of MGP, H_{MGP}, is $2H$. The motion equations of the two machines are given by (9) and (10).

$$\begin{cases} s\Delta\omega_M = \dfrac{1}{2H}(\Delta T_{eM} - \Delta T_{mM} - K_{DM}\Delta\omega_M) \\ s\Delta\delta_M = \omega_0\Delta\omega_M \end{cases} \tag{9}$$

$$\begin{cases} s\Delta\omega_G = \dfrac{1}{2H}(\Delta T_{mG} - \Delta T_{eG} - K_{DG}\Delta\omega_G) \\ s\Delta\delta_G = \omega_0\Delta\omega_G \end{cases} \tag{10}$$

The damping terms, $K_{DM}\Delta\omega_M$ and $K_{DG}\Delta\omega_G$, of those two machines are the same due to the same rotor angular speed. The frequency differences between the stator and the rotor of the SM and the SG are also usually equal. Then we define that $\omega_{MGP} = \omega_M = \omega_G$ where ω_{MGP} is the rotor speed of MGP. Hence, the speed in (9) and (10) can be added directly. Combining the definition of deviation of power angle of the MGP, $\Delta\delta_{MG}$, the motion equation of the MGP described by $\Delta\omega_{MGP}$ and $\Delta\delta_{MG}$ can be expressed as (11).

$$\begin{cases} s\Delta\omega_{MGP} = \dfrac{1}{2H_{MGP}}[\Delta T_{eM} - \dfrac{K_{sM}K_{sG}}{(K_{sM}+K_{sG})}\Delta\delta_{MG} \\ \quad -(K_{DM}+K_{DG})\Delta\omega_{MGP}] \\ s\Delta\delta_{MG} = \dfrac{K_{sM}+K_{sG}}{K_{sM}}\omega_0\Delta\omega_{MGP} \end{cases} \tag{11}$$

B. FREQUENCY RESPONSE CHARACTERISTIC OF A SINGLE MGP

The frequency response characteristic of a single MGP based on Fig.4 is studied in this section. The frequency response characteristic refers to the dynamic frequency response of power grids to the active power fluctuation. RESs are decoupled from the grid frequency with traditional vector control. Therefore, the dynamic characteristics of RES are not emphasized.

Similar to the classical small signal model for synchronous generators [28], the simplified small signal model of the MGP system can be built as (12). In which, the disturbance variable ΔT_{eM} is the input disturbance Δu, and the rotor speed deviation $\Delta\omega_{MGP}$ is the output Δy.

$$\begin{bmatrix} s\Delta\omega_{MGP} \\ s\Delta\delta_{MG} \\ \Delta y \end{bmatrix} = \begin{bmatrix} \dfrac{-(K_{DM}+K_{DG})}{2H_{MGP}} & \dfrac{-1}{2H_{MGP}} & \dfrac{K_{sM}K_{sG}}{(K_{sM}+K_{sG})} & \dfrac{1}{2H_{MGP}} \\ \dfrac{(K_{sM}+K_{sG})\omega_0}{K_{sM}} & 0 & 0 \\ 1 & 0 & 0 \end{bmatrix} \times \begin{bmatrix} \Delta\omega_{MGP} \\ \Delta\delta_{MG} \\ \Delta u \end{bmatrix} = \begin{bmatrix} a_{11} & a_{12} & b_{13} \\ a_{21} & a_{22} & b_{23} \\ c_{31} & c_{32} & d_{33} \end{bmatrix} \begin{bmatrix} \Delta\omega_{MGP} \\ \Delta\delta_{MG} \\ \Delta u \end{bmatrix} \tag{12}$$

The closed-loop transfer function $G_{MGP}(s)$ from the disturbance variable ΔT_{eM} to the output $\Delta\omega_{MGP}$ is given in (13).

$$\frac{\Delta y}{\Delta u} = G_{MGP}(s) = \frac{\Delta\omega_{MGP}}{\Delta T_{eM}} = C_{sys}(sI - A_{sys})^{-1}B_{sys} + D_{sys} \tag{13}$$

where I is the identity matrix, the transfer function $G_{MGP}(s)$ represents the frequency response characteristic of the system over the full frequency band, $C_{sys} = [c_{31}c_{32}] = [10]$, $D_{sys} = d_{33} = 0$.

A_{sys}, B_{sys} are calculated as follows.

$$A_{sys} = \begin{bmatrix} a_{11} & a_{12} \\ a_{21} & a_{22} \end{bmatrix} = \begin{bmatrix} \dfrac{-1}{2H_{MGP}}(K_{DM}+K_{DG}) & \dfrac{-1}{2H_{MGP}}\dfrac{K_{sG}K_{sM}}{(K_{sG}+K_{sM})} \\ \dfrac{(K_{sG}+K_{sM})\omega_0}{K_{sM}} & 0 \end{bmatrix} \tag{14}$$

$$B_{sys} = \begin{bmatrix} b_{13} \\ b_{23} \end{bmatrix} = \begin{bmatrix} \dfrac{1}{2H_{MGP}} \\ 0 \end{bmatrix} \tag{15}$$

The Bode diagrams of the closed-loop transfer function of a single SG and a single MGP under the same parameters is shown as in Fig.5(a), and the time-domain response of frequency under the same disturbance are shown in Fig.5(b). It can be seen that the MGP and SG have similar frequency curves, and the MGP has stronger frequency disturbance suppression ability than a single generator, mainly because of its larger inertia and damping parameters with the same capacity.

IV. THE PROMOTION EFFECT OF MGP ON THE UPPER LIMIT PENETRATION RATE OF RES

A. SFR MODEL OF MULTI-MACHINE SYSTEMS IN WHICH RES IS CONNECTED TO THE GRID VIA MGP

The SFR model averages the dynamic behavior of machines in a large system into an equivalent single machine without considering the specific governor control, turbine model, limiting and other nonlinear links with the secondary frequency regulation, it is often used to describe the average system frequency response after a disturbance in power systems [29], [30]. Thus, the SFR model is established to quantify the effects of MGP on the frequency response of in a system.

For power systems with high penetration of RES, it is necessary to introduce a parameter to characterize the penetration rate of RES. The proportion of RES can be defined as (16).

$$K = \frac{\text{Power output of RES}}{\text{Load power of system}} \tag{16}$$

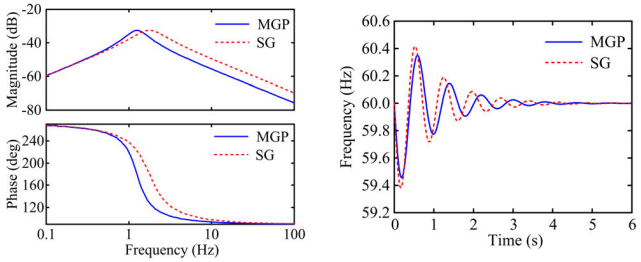

FIGURE 5. Frequency characteristic of a single MGP and a single SG. (a) Bode diagrams of closed-loop transfer functions of a single SG and a single MGP. (b) Time-domain frequency response of a single SG and a single MGP under the same disturbance.

Based on the traditional vector control, the inertial support of RES is completely provided by MGP. The inertial characteristic of MGP in Section II shows that the moment of inertia of MGP is about 65% of the traditional generator unit with the same capacity, i.e., $H_{\mathrm{MGP}} = 0.65H_{\mathrm{G}}$, where H_{MGP} is the inertial constant of MGP and H_{G} is the inertia constant of the traditional generator unit with the same capacity. Assuming that all RES are connected to grids with MGP, the K ratio RES with MGP can provide additional inertia of $0.65K \cdot H_{\mathrm{G}}$. Combined with (11), K ratio RES with MGP can provide additional damping $2K \cdot D$. Also, the goal of this paper is to study the overall frequency characteristics of the system integrated with MGPs, so the frequency dispersion, power angle stability issues, and uncertainty of the RES are not considered with the SFR model. Therefore, the simplified aggregated SFR model of the power system with the K proportion of RES connected to grids via MGP can be obtained as shown in Fig.6, where D is the damping factor, R is the governor regulator coefficient, T_{R} is the reheater time constant, F_{H} is fraction of total power generated by the high-pressure turbine, ΔP_{L} is the load power deviation, ΔP_{m} is the mechanical power deviation of generator units, and ΔP_{e} is the electromagnetic power deviation of generator units.

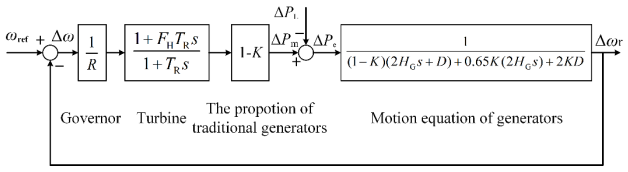

FIGURE 6. SFR model of the power system with the K proportion of RES connected to grids through MGP.

The open-loop transfer function of the system in Fig.6 relating the output $\Delta\omega_{\mathrm{r}}$ and the input ω_{ref} can be deduced as (17).

$$H(s) = \frac{1-K}{R}\frac{1+F_{\mathrm{H}}T_{\mathrm{R}}s}{1+T_{\mathrm{R}}s} \times \frac{1}{(1-K)(2H_{\mathrm{G}}s+D)+0.65K(2H_{\mathrm{G}}s)+2KD} = \frac{(1-K)F_{\mathrm{H}}}{R}\frac{s+\frac{1}{F_{\mathrm{H}}T_{\mathrm{R}}}}{s^2+(\frac{1}{T_{\mathrm{R}}}+\frac{2KD}{2H_{\mathrm{G}}-0.7KH_{\mathrm{G}}})s+\frac{2KD}{T_{\mathrm{R}}(2H_{\mathrm{G}}-0.7KH_{\mathrm{G}})}} \tag{17}$$

The closed-loop of frequency response with a given power disturbance can be deduced as (18).

$$\begin{aligned} G(s) &= \frac{\Delta\omega_r}{\Delta P_{\mathrm{L}}} = \frac{\frac{1}{(1-K)(2H_{\mathrm{G}}s+D)+0.65K(2H_{\mathrm{G}}s)+2KD}}{1+H(s)} \\ &= \frac{1}{(1-K)(2H_{\mathrm{G}}s+D)+0.65K(2H_{\mathrm{G}}s)+2KD+\frac{1-K}{R}\frac{1+F_{\mathrm{H}}T_{\mathrm{R}}s}{1+T_{\mathrm{R}}s}} \\ &= \frac{R\omega_{\mathrm{n}}^2}{DKR+DR+(1-K)}\frac{1+T_{\mathrm{R}}s}{s^2+2\varsigma\omega_{\mathrm{n}}s+\omega_{\mathrm{n}}^2} \end{aligned} \tag{18}$$

where the natural oscillation frequency ω_{n} and the damping ratio ζ are given by (19) and (20).

$$\omega_{\mathrm{n}}^2 = \frac{DKR+DR+(1-K)}{2H_{\mathrm{G}}RT_{\mathrm{R}}-0.7H_{\mathrm{G}}KRT_{\mathrm{R}}} \tag{19}$$

$$\varsigma = \frac{1}{2}\frac{2H_{\mathrm{G}}R-0.7RH_{\mathrm{G}}K+(DRK+DR+(1-K)F_{\mathrm{H}})T_{\mathrm{R}}}{DKR+DR+(1-K)}\omega_{\mathrm{n}} \tag{20}$$

In the Laplace domain, per unit frequency can be computed for ΔP_{L} in the form of a step function amplitude P_{step} of the system as shown in (21).

$$\Delta\omega_r(s) = \frac{R\omega_{\mathrm{n}}^2}{DKR+DR+(1-K)}\left(\frac{(1+T_{\mathrm{R}}s)P_{\mathrm{Step}}}{s\left(s^2+2\varsigma\omega_{\mathrm{n}}s+\omega_{\mathrm{n}}^2\right)}\right) \tag{21}$$

Consequently, the frequency deviation in the time domain $\Delta\omega_{\mathrm{r}}(t)$ is given by as in (22), shown at the bottom of the next page, where the coefficients α, the damped frequency ω_{fr}, and ϕ are calculated as follows.

$$\alpha = \sqrt{\frac{1-2T_{\mathrm{R}}\varsigma\omega_{\mathrm{n}}+T_{\mathrm{R}}^2\omega_{\mathrm{n}}^2}{1-\varsigma^2}} \tag{23}$$

$$\omega_{\mathrm{fr}} = \omega_{\mathrm{n}}\sqrt{1-\varsigma^2} \tag{24}$$

$$\phi = \tan^{-1}\left(\frac{\omega_{\mathrm{fr}}T_{\mathrm{R}}}{1-\varsigma\omega_{\mathrm{n}}T_{\mathrm{R}}}\right)-\tan^{-1}\left(\frac{\sqrt{1-\varsigma^2}}{-\varsigma}\right) \tag{25}$$

According to the Laplace domain and time domain solutions of frequency response of the system after a load disturbance in the form of a step function, the relationship between key dynamic frequency indices and the proportion of RES connected to grids via MGP can be obtained. The key dynamic frequency indices include the initial rate of change of frequency (RoCoF), the steady-state deviation of frequency response ($\Delta f_{\mathrm{ssMGP}}$) and the maximum frequency deviation ($\Delta f_{\mathrm{nadirMGP}}$) for power systems whose RES is with MGP.

Corresponding to the condition $t = 0$ in (22), the RoCoF for power systems whose RES is with MGP $RoCoF_{\mathrm{MGP}}$ is

given in (26).

$$\begin{aligned} RoCoF_{\mathrm{MGP}} &= \lim_{t\to 0^+}\frac{d\Delta\omega_r(t)}{dt} = \lim_{s\to+\infty} s^2\Delta\omega_r(s) \\ &= \lim_{s\to+\infty} s^2\frac{R\omega_{\mathrm{n}}^2}{(DKR+DR+1-K)} \\ &\quad\times\left(\frac{(1+T_{\mathrm{R}}s)\,P_{\mathrm{Step}}}{s\left(s^2+2\varsigma\omega_{\mathrm{n}}s+\omega_{\mathrm{n}}^2\right)}\right) \\ &= \frac{P_{\mathrm{Step}}}{2H_{\mathrm{G}}(1-0.35K)} \end{aligned} \tag{26}$$

Corresponding to the condition $t=\infty$ for (22), $\Delta f_{\mathrm{ssMGP}}$ is given in (27).

$$\begin{aligned} \Delta f_{\mathrm{ssMGP}} &= \lim_{t\to+\infty}\Delta\omega_r(t) = \lim_{s\to 0^+} s\Delta\omega_r(s) \\ &= \lim_{s\to 0^+} s\frac{R\omega_n^2}{(DKR+DR+1-K)} \\ &\quad\times\left(\frac{(1+T_{\mathrm{R}}s)\,P_{\mathrm{Step}}}{s\left(s^2+2\varsigma\omega_{\mathrm{n}}s+\omega_{\mathrm{n}}^2\right)}\right) \\ &= \frac{RP_{\mathrm{Step}}}{DKR+DR+(1-K)} \end{aligned} \tag{27}$$

At the frequency nadir f_{nadirMGP}, the derivative of the frequency is 0, as shown in (28) and (29).

$$\begin{cases} \dfrac{d\Delta\omega_r(t)}{dt}=0 \\ t_{nadir}=\dfrac{1}{\omega_{\mathrm{fr}}}\tan^{-1}\left(\dfrac{\omega_{\mathrm{fr}}T_{\mathrm{R}}}{\varsigma\omega_{\mathrm{n}}T_{\mathrm{R}}-1}\right) \end{cases} \tag{28}$$

$$\begin{aligned} \Delta f_{\mathrm{nadirMGP}} &= \Delta\omega_r(t)|_{t=t_{\mathrm{nadir}}} \\ &= \frac{RP_{\mathrm{Step}}\left[1+\alpha e^{-\varsigma\omega_n t_{\mathrm{nadir}}}\sin\left(\omega_{\mathrm{fr}}t_{\mathrm{nadir}}+\phi\right)\right]}{DKR+DR+(1-K)} \end{aligned} \tag{29}$$

In order to compare the effect of MGP on frequency stability, this paper derives three key dynamic frequency indices, RoCoF ($RoCoF_{\mathrm{new}}$), the steady-state deviation of frequency response ($\Delta f_{\mathrm{ssnew}}$) and the maximum frequency deviation ($\Delta f_{\mathrm{nadirnew}}$) for power systems whose RES is without MGP accounts for K as shown in (30), (31) and (32). The specific derivation process is shown in Appendix B.

$$\begin{aligned} ROCOF_{\mathrm{new}} &= \lim_{t\to 0^+}\frac{d\Delta\omega_r(t)}{dt} = \lim_{s\to+\infty} s^2\Delta\omega_r(s) \\ &= \lim_{s\to+\infty} s^2\frac{R\omega_{\mathrm{n}}^2}{DR+1-K} \\ &\quad\times\left(\frac{(1+T_{\mathrm{R}}s)\,P_{\mathrm{Step}}}{s\left(s^2+2\varsigma\omega_{\mathrm{n}}s+\omega_{\mathrm{n}}^2\right)}\right) \\ &= \frac{P_{\mathrm{Step}}}{2H_{\mathrm{G}}(1-K)} \end{aligned} \tag{30}$$

$$\begin{aligned} \Delta f_{\mathrm{ssnew}} &= \lim_{t\to+\infty}\Delta\omega_r(t) = \lim_{s\to 0^+} s\Delta\omega_r(s) \\ &= \lim_{s\to 0^+}\frac{R\omega_{\mathrm{n}}^2}{DR+1-K}\left(\frac{(1+T_R s)\,P_{\mathrm{Step}}}{\left(s^2+2\varsigma\omega_{\mathrm{n}}s+\omega_{\mathrm{n}}^2\right)}\right) \\ &= \frac{RP_{\mathrm{Step}}}{DR+(1-K)} \end{aligned} \tag{31}$$

$$\begin{aligned} \Delta f_{\mathrm{nadirnew}} &= \Delta\omega_r(t)|_{t=t_{\mathrm{nadir}}} \\ &= \frac{RP_{\mathrm{Step}}}{DR+(1-K)}(1+\sqrt{1-\varsigma^2}\alpha e^{-\varsigma\omega_{\mathrm{n}}t_{\mathrm{nadir}}}) \end{aligned} \tag{32}$$

For the typical parameter scenario ($R=5\%$, $H_{\mathrm{G}}=12.0$s, $T_{\mathrm{R}}=6$s, $F_{\mathrm{H}}=0.333$, $D=0.01$ p.u. power/p.u. speed deviation) [30], the key dynamic frequency indices of RES connected to grids with and without MGP are calculated. The results are listed in Table 1, and the key indices with typical values of K and the critical penetration rate of RES are calculated in Table 2. It can be concluded that.

1) RoCoF is inversely proportional to the inertia constant of the system, and MGP can significantly reduce the RoCoF. Also, the frequency nadir is improved with MGP. While the steady-state frequency is less sensitive.
2) The constraint of the critical penetration rate of RES is that the frequency response after a 0.1 p.u. load disturbance does not exceed 0.02 p.u. Constrained by Δf_{ss}, the critical rate of RES without MGP is 75%, and is 75.9% with MGP, under typical parameters.
3) Constrained by $\Delta f_{\mathrm{nadir}}$, the critical penetration of RES without MGP is 52%, and is 66.7% with MGP.

TABLE 1. Key dynamic frequency indices of the system frequency response based on the SFR model.

Key indices	RES	RES+MGP
RoCoF	1/24(1-K)	1/(24-16.8K)
Steady-state deviation Δf_{ss}	0.05/[0.0005+(1-K)]	0.05/[0.0005+(1-K)+0.0005K]
Maximum deviation $\Delta f_{\mathrm{nadir}}$	0.05*[1+2.57*$e^{-1.0429}$]/[0.0005+(1-K)]	0.05*[1+0.625*$e^{-0.794}$]/[0.0005+(1-K)+0.0005K]

B. TIME-DOMAIN ANALYSIS FOR SYSTEM FREQUENCY RESPONSE OF MULTI-MACHINE SYSTEMS WITH HIGH PENETRATION OF RES

Two simulation models are built in PSCAD/EMTDC to analyze the frequency characteristics of high-penetrate RES systems with and without MGP. As shown in Fig.7, in model I, the PV is directly connected to grids, and in model II, the PV is connected to grids through the MGP system. Regardless

$$\begin{aligned} \Delta\omega_r(t) &= \frac{RP_{\mathrm{Step}}[1+\frac{(T_{\mathrm{R}}\omega_{\mathrm{n}}^2-\varsigma\omega_{\mathrm{n}})\sin\left(\omega_{\mathrm{n}}\sqrt{\varsigma^2-1}t\right)e^{-\varsigma\omega_{\mathrm{n}}t}}{\omega_n\sqrt{\varsigma^2-1}}-\cos\left(\omega_{\mathrm{n}}\sqrt{\varsigma^2-1}t\right)e^{-\varsigma\omega_{\mathrm{n}}t}]}{DKR+DR+(1-K)} \\ &= \frac{RP_{\mathrm{Step}}}{DKR+DR+(1-K)}\left[1+\alpha e^{-\varsigma\omega_{\mathrm{n}}t}\sin\left(\omega_{\mathrm{fr}}t+\phi\right)\right] \end{aligned} \tag{22}$$

TABLE 2. Key dynamic frequency indices of the system frequency response in typical penetration rate of RES.

Key indices/ penetration	RES			RES+MGP		
	25%	50%	75%	25%	50%	75%
RoCoF	0.056	0.083	0.167	0.051	0.064	0.088
Δf_{ss}	0.067	0.1	0.2	0.067	0.1	0.19
Δf_{nadir}	0.127	0.19	0.38	0.085	0.128	0.256
Critical penetration rate (Δf_{ss})	75%			75.9%		
Critical penetration rate (Δf_{nadir})	52%			66.7%		

of the frequency regulating effect of PV, the frequency responses of the two models under different penetration rates of PV are compared to study the frequency stability. The specific parameters of simulation models are presented in Appendix C. The detailed control diagram of PV and MGP adopted in simulation model I and model II are shown in Appendix D.

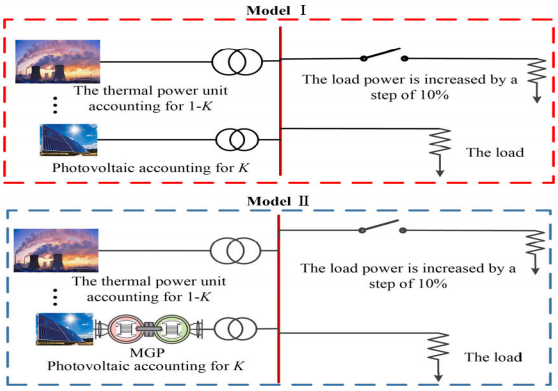

FIGURE 7. Simulation models of the influence of MGP on frequency response characteristics.

In the three scenarios, the proportion of PV is 25%, 50% and 75%, while the load power is increased by a step of 10% respectively. The active powers transmitted by thermal power units and PV units under different proportions are shown in Fig.8.

From Fig.8, it can be seen that there are two roles for the inertial response of the MGP: 1) providing the instantaneous active power support at the moment of load disturbance. 2) improved with the increased power transmission of PV.

Fig.9 shows the frequency-time responses in the two models under the three scenarios. From Fig.9, the key dynamic frequency indices of PV connected to grids with and without MGP are listed in Table 3.

We can conclude that:

1) The dynamic change of the system frequency worsens as the penetration of PV increases.
2) Under the same proportion of PV, for simulation model II in which PV is connected to grids through the MGP, the RoCoF is lower, the maximum frequency deviation

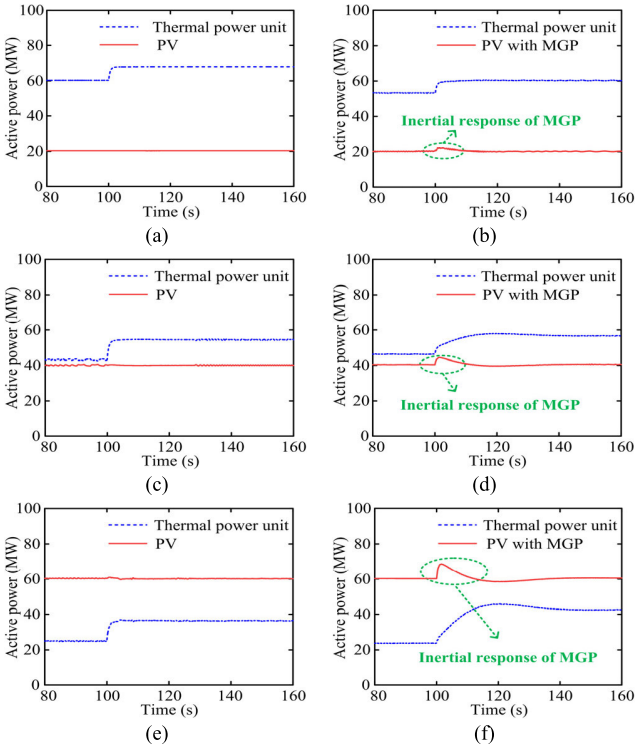

FIGURE 8. Comparison of the active power transmitted by traditional thermal power unit and PV with different proportions. (a) 75% thermal power unit and 25% PV without MGP. (b) 75% thermal power unit and 25% PV with MGP. (c) 50% thermal power unit and 50% PV without MGP. (d) 50% thermal power unit and 50% PV with MGP. (e) 25% thermal power unit and 75% PV without MGP. (f) 25% thermal power unit and 75% PV with MGP.

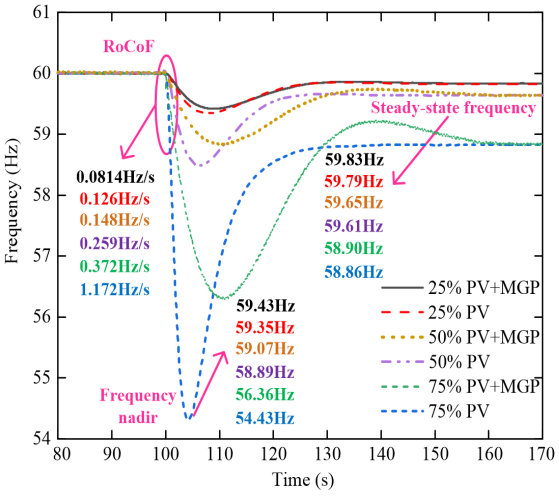

FIGURE 9. Frequency-time responses in the two models under three scenarios.

Δf_{nadir} becomes smaller obviously, and the steady-state deviation Δf_{ss} changes smaller compared with model I.

3) After a 10% increase in load power with a step change, the Δf_{ss} of model I under 75% penetration ratio of PV is 1.14 Hz and the Δf_{ss} of model II under 75% penetration ratio of PV with MGP is 1.10 Hz; the Δf_{nadir} of model I

TABLE 3. Key dynamic frequency indices of PV connected to grids with and without MGP.

Key indices	RoCoF (Hz/s)	Maximum deviation Δf_{nadir} (Hz)	Steady-state deviation Δf_{ss} (Hz)
25% PV connected to grids via MGP	0.0815	0.57	0.17
25% PV connected to grids directly	0.126	0.65	0.21
50% PV connected to grids via MGP	0.148	0.93	0.35
50% PV connected to grids directly	0.259	1.11	0.39
75% PV connected to grids via MGP	0.372	3.64	1.10
75% PV connected to grids directly	1.172	5.57	1.14

under 50% penetration ratio of PV is 1.11 Hz and the Δf_{nadir} of model II under 50% penetration ratio of PV with MGP is 0.93 Hz. According to the constraint that frequency response after a 10% p.u. load disturbance does not exceed 0.02 p.u., the simulations agree with the predicted results in Table 1.

4) The MGP system clearly improves frequency stability based on the three key indices of dynamic frequency response.

V. EXPERIMENTAL VERIFICATION OF ENHANCED INFLUENCE OF MGP ON TIME DOMAIN FREQUENCY CURVES

In order to validate the enhanced influence of MGP on the time domain frequency response and the system frequency dynamic response of power systems with RES connected to the grid via MGP, experimental analysis is carries out in this section.

A. TESTING ON TIME DOMAIN FREQUENCY RESPONSE OF A SINGLE MGP

An experimental MGP test bench is established, as shown in Fig.10, where one of the tasks is to test the frequency characteristic of the MGP.

In this test bench, a PV simulator is used to simulate the real renewable power generation, and the MGP system consists of two 5.5 kW synchronous machines. The RES is connected to the programable load via the MGP when switches k1, k2 are closed and k4 is open. The electrical quantities transducer measures the power transmission through the MGP system, and the programmable logic controller (PLC) controls the power tracking of PV and power output of the MGP system.

The test bench can be also used to emulate a SG for comparison study while switches k1 and k2 are open and switch k4 is closed. A 5.5 kW DC machine is connected mechanically with the SG, and the DC speed governor drives the DC machine and SG to mimic the SG unit. With switch k3 closed, the SG is connected to the programmable load. The specific parameters of the above machines are shown in Appendix E. Load disturbances are set in the programmable load, and frequency response in the two experimental settings under load disturbances can be recorded.

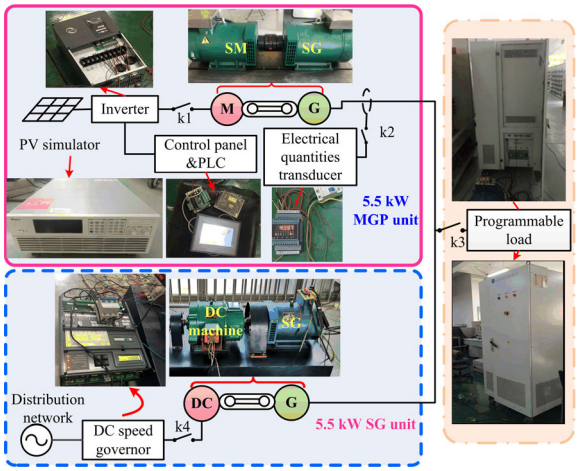

FIGURE 10. 5.5 kW experimental bench.

The frequency response results of the 5.5 kW MGP and the 5.5 kW SG under load changes from 0 to 1200 W and from 1200 W to 3000 W are shown in Fig.11. It can be seen that the MGP and a single SG have similar frequency response under the same disturbance, and the MGP system has stronger frequency disturbance suppression ability than a single SG with the same capacity.

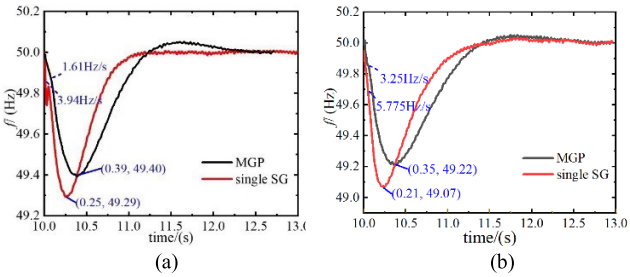

FIGURE 11. Frequency response of two experimental settings. (a) Load disturbance from 0 to 1200 W. (b) Load disturbance from 1200 W to 3000 W.

B. EXPERIMENTAL ANALYSIS FOR SYSTEM FREQUENCY RESPONSE OF MULTI-MACHINE SYSTEMS WITH MGP

To analyze the frequency characteristics of multi-machine system with and without MGP, the experimental system is built according to the structure of Fig. 7. As shown in Fig.12, the PV simulator and traditional SG are connected to the load with switches k1, k2 and k3 closed at the same time, similar to the structure of model I, in which PV is connected to grids directly. In addition, closing all the switches k1, k2, k3 and k4 in Fig.10 can simulate the structure of model II, in which the PV is connected to grids through MGP.

In the two experimental models, the output of PV is set to 1500W and 2100W respectively to imitate different

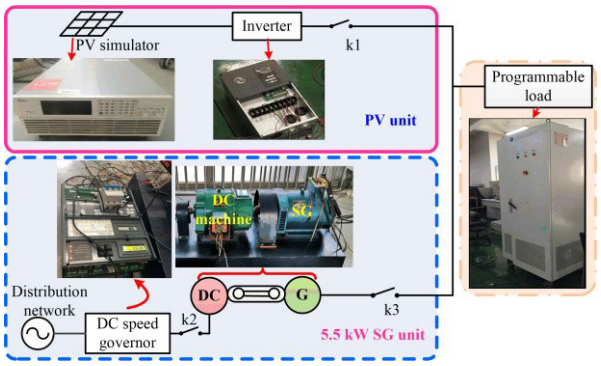

FIGURE 12. The PV simulator and traditional SG experimental bench.

proportions of PV, and the remaining active output is borne by the SG. The load is set to suddenly increase from 2100W to 3000W, measuring the output curves of PV and SG in the two experimental models, as shown in Fig.13.

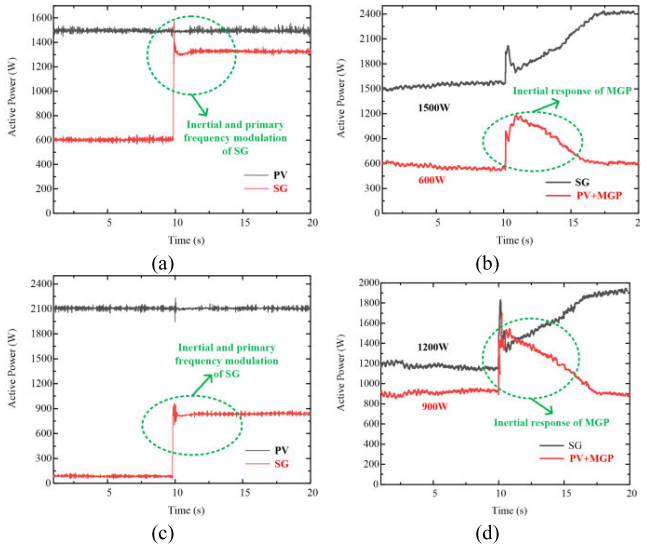

FIGURE 13. Comparison of the active powers transmitted by SG unit and PV under different proportions. (a) 1500W PV without MGP. (b) 1500W PV with MGP. (c) 2100W PV without MGP. (d) 2100W with MGP.

In the model I of Fig.12, the initial power of load is 2100 and the power of SG is 600W with the output of PV set 1500W. When the load power increased suddenly from 2100W to 3000W, the inertial and primary frequency of SG complement the power shortage of load, as shown in Fig.13(a). In the experimental model II, the initial power of PV with MGP is 600W when the output of PV is set 1500W because of the loss of MGP. When the load power increased suddenly from 2100W to 3000W, the inertial and primary frequency of SG and the inertial response of MGP complement the power shortage of load simultaneously, as shown in Fig.13(b). When the photovoltaic power is set to 2100, the power curves of model I and model II are shown in Fig.13(c) and (d) respectively.

The frequency response curves of two models with different power outputs of PV are shown in Fig.14. By comparing the RoCoF and the frequency nadir, the dynamic change of system frequency response becomes worse with the increased power from PV.

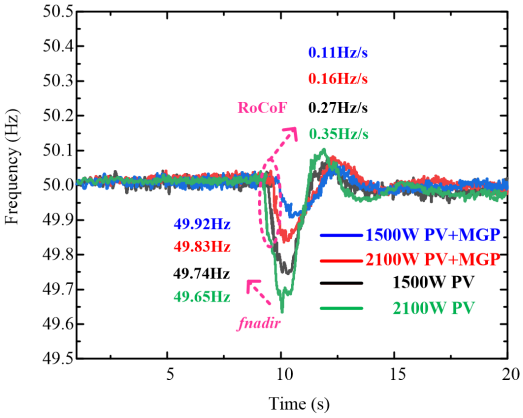

FIGURE 14. Frequency-time responses in the two models under three scenarios.

From Fig.13 and Fig.14, it can be seen that PV with MGP can provide instantaneous active power support because of the inertial response of MGP at the moment of load disturbance. And the inertial support provided by MGP can improve the dynamic index of system frequency response.

VI. CONCLUSION

Considering the frequency instability caused by the lack of inertial response in the power grid with high penetration of RES, a renewable grid-connection method of MGP is proposed. This paper compares the frequency responses of high penetration of RES with and without the MGP, mainly considering the difference caused by the inertia effect. The following are the main conclusions:

1) The frequency response characteristic of MGP is derived in a single-machine infinite bus system, and the response characteristic is validated by an example.
2) The SFR model for the MGP is built, and three key indices (RoCoF, steady-state frequency deviation, and maximum frequency deviation) are analyzed and calculated. The results show that the inertial response of the MGP increases the upper limit penetration rate of RES connected to the grid.
3) A simulation model is built to compare the time-domain of the frequency response curves of the PV connected to the grid under 25%, 50%, and 75% penetration ratios, with and without MGP. The simulation result verified the theoretical analysis.
4) Experimental analysis of a single MGP experimental setup and a multi-machine experimental bench validates the enhanced influence of MGP on the frequency response.

APPENDIX A

See Tables 4 and 5.

TABLE 4. Inertia moment of 600 MVA thermal power unit.

Mass composition	Inertia moment ($kg \cdot m^2$)	Total moment of inertia ($kg \cdot m^2$)
Exciter	58.36	22713.22
Generator	7435.81	
Low pressure cylinder	13112.76	
High pressure cylinder	2106.29	

TABLE 5. Inertia moment of 600 MVA MGP.

Mass composition	Inertia moment ($kg \cdot m^2$)	Total moment of inertia ($kg \cdot m^2$)
Exciter of the SM	58.36	14988.34
Rotor of the SM	7435.81	
Exciter of the SG	58.36	
Rotor of the SG	7435.81	

APPENDIX B

The simplified aggregate SFR model of the power system with K proportion of RES is shown as in Fig.15.

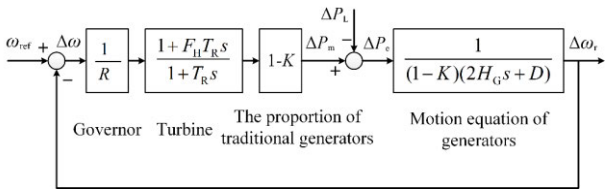

FIGURE 15. SFR model of the power system with K proportion of RES.

The open-loop transfer function of the system shown in Fig.15 is given by (33).

$$H(s) = \frac{1-K}{R}\frac{1+F_H T_R s}{1+T_R s}\frac{1}{(1-K)(2H_G s+D)} \tag{33}$$

The closed-loop of frequency response with a given power disturbance can be deduced as follows.

$$\begin{aligned} G(s) &= \frac{\Delta\omega_r}{\Delta P_L} = \frac{\frac{1}{(1-K)(2H_G s+D)}}{1+H(s)} \\ &= \frac{R\omega_n^2}{(DR+1-K)}\frac{1+T_R s}{s^2+2\varsigma\omega_n s+\omega_n^2} \end{aligned} \tag{34}$$

$$\omega_n^2 = \frac{DR+1-K}{H_G R T_R (1-K)} \tag{35}$$

$$\varsigma = \frac{H_G R(1-K)+(DR+F_H(1-K))T_R}{2(DR+1-K)}\cdot\omega_n \tag{36}$$

In the Laplace domain, the frequency response after a load disturbance in the form of a step function amplitude P_{step} is derived as (37).

$$\Delta\omega_r(s) = \frac{R\omega_n^2}{DR+1-K}\left(\frac{(1+T_R s)P_{Step}}{s\left(s^2+2\varsigma\omega_n s+\omega_n^2\right)}\right) \tag{37}$$

The corresponding time domain analytical solution is determined as in (38), shown at the top of the next page.

APPENDIX C

See Tables 6 and 7.

TABLE 6. The parameters of simulation model I.

Basic data	25% PV	50% PV	75% PV
Load power (MW)	80	80	80
Installed capacity of thermal power unit (MVA)	75	50	75
Installed capacity of PV (MVA)	25	50	25
Inertia constant of thermal power unit (s)	12.45	8.31	4.15
Inertia constant of PV (s)	0	0	0
Inertia constant of the system (s)	12.45	8.31	4.15

TABLE 7. The parameters of simulation model II.

Basic data	25% PV	50% PV	75% PV
Load power (MW)	80	80	80
Installed capacity of thermal power unit (MVA)	75	50	75
Installed capacity of PV with MGP (MVA)	25	50	25
Inertia constant of thermal power unit (s)	12.45	8.31	4.15
Inertia constant of PV with MGP (s)	2.7	5.4	8.1
Inertia constant of the system (s)	15.15	13.71	12.24

APPENDIX D

See Figs. 16 and 17.

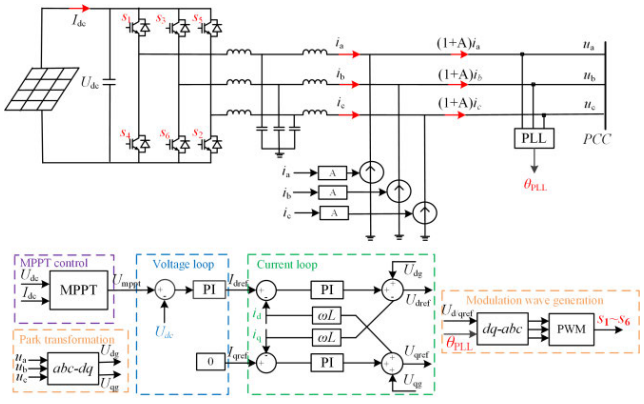

FIGURE 16. The detailed control diagram of PV in model I.

APPENDIX E

See Table 8.

$$\Delta\omega_r(t) = \frac{RP_{\text{Step}}[1 + \frac{(T_R\omega_n^2 - \varsigma\omega_n)\sin\left(\omega_n\sqrt{\varsigma^2-1}t\right)e^{-\varsigma\omega_n t}}{\omega_n\sqrt{\varsigma^2-1}} - \cos\left(\omega_n\sqrt{\varsigma^2-1}t\right)e^{-\varsigma\omega_n t}]}{(DR+1-K)}$$
$$= \frac{RP_{\text{Step}}}{(DR+1-K)}\left[1 + \alpha e^{-\varsigma\omega_n t}\sin(\omega_{\text{fr}}t + \phi)\right] \quad (38)$$

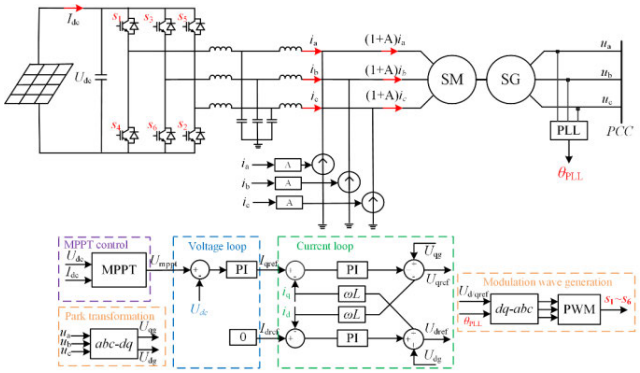

FIGURE 17. The detailed control diagram of MGP in model II.

TABLE 8. Equipment parameters of experimental system.

Equipment	Model number	Main parameters	
SM / SG	TF(D)21/10 .5-4	Rated power (kW)	5.5
		Rated voltage (V)	230
		Rated current (A)	9
		Rated frequency (Hz)	50
		Rated power factor	0.8
		Rated speed (RPM)	1500
		Field current (A)	3.9
DC machine	Z2-52	Rated power (kW)	5.5
		Rated voltage (V)	220
		Rated current (A)	41.1
		Excitation voltage (V)	220
		Excitation current (A)	1.18
		Excitation mode	separately
		Rated speed (RPM)	1500
PV emulator	62100H-600S	Rated power (kW)	10
		Output-voltage (V)	0~600
		Output-current (A)	0~17
Inverter	BOS BNSG10KS	Rated power (kW)	10
		DC voltage (Vdc)	400~780
		AC voltage (Vac)	310~450
		Input	AC3PF
Frequency converter	ZY-P800F-5.5K-3B	Rated input voltage (V)	380
		Rated frequency (Hz)	50/60
		Rated output current (A)	17
PLC control panel		CPU224XP/FX1N-20MR-4AD	
Speed governor		590P/0380/500/0041/UK/AN/230/0	
AC load	ACLT-3803H program-mable load	Frequency (Hz)	50
		Input voltage (V)	400
		Rated resistive power (kW)	33.33
		Rated inductive power (kVar)	33.33
		Rated capacitive power (kVar)	33.33
Waveform Recorder		YOKOGAWA-DL850E	

REFERENCES

[1] T. Li, Y. Li, S. Li, and W. Zhang, "Research on current-limiting control strategy suitable for ground faults in AC microgrid," *IEEE J. Emerg. Sel. Topics Power Electron.*, vol. 9, no. 2, pp. 1736–1750, Mar. 2020.

[2] J. M. Kennedy, B. Fox, T. Littler, and D. Flynn, "Validation of fixed speed induction generator models for inertial response using wind farm measurements," *IEEE Trans. Power Syst.*, vol. 26, no. 3, pp. 1454–1461, Aug. 2011.

[3] D. Ochoa and S. Martinez, "Fast-frequency response provided by DFIG-wind turbines and its impact on the grid," *IEEE Trans. Power Syst.*, vol. 32, no. 5, pp. 4002–4011, Sep. 2017.

[4] M. Altin, A. D. Hansen, T. K. Barlas, K. Das, and J. N. Sakamuri, "Optimization of short-term overproduction response of variable speed wind turbines," *IEEE Trans. Sustain. Energy*, vol. 9, no. 4, pp. 1732–1739, Oct. 2018.

[5] M. C. Chandorkar, D. M. Divan, and R. Adapa, "Control of parallel connected inverters in standalone AC supply systems," *IEEE Trans. Ind. Appl.*, vol. 29, no. 1, pp. 136–143, Jan./Feb. 1993.

[6] X. Meng, J. Liu, and Z. Liu, "A generalized droop control for grid-supporting inverter based on comparison between traditional droop control and virtual synchronous generator control," *IEEE Trans. Power Electron.*, vol. 34, no. 6, pp. 5416–5438, Jun. 2019.

[7] J. Liu, Y. Miura, and T. Ise, "Comparison of dynamic characteristics between virtual synchronous generator and droop control in inverter-based distributed generators," *IEEE Trans. Power Electron.*, vol. 31, no. 5, pp. 3600–3611, May 2016.

[8] S. Ghosh, S. Kamalasadan, N. Senroy, and J. Enslin, "Doubly fed induction generator (DFIG)-based wind farm control framework for primary frequency and inertial response application," *IEEE Trans. Power Syst.*, vol. 31, no. 3, pp. 1861–1871, May 2016.

[9] D. Ochoa and S. Martinez, "Frequency dependent strategy for mitigating wind power fluctuations of a doubly-fed induction generator wind turbine based on virtual inertia control and blade pitch angle regulation," *Renew. Energy*, vol. 128, pp. 108–124, Dec. 2018.

[10] A. Fathi, Q. Shafiee, and H. Bevrani, "Robust frequency control of microgrids using an extended virtual synchronous generator," *IEEE Trans. Power Syst.*, vol. 33, no. 6, pp. 6289–6297, Nov. 2018.

[11] K. Jiang, H. Su, H. Lin, K. He, H. Zeng, and Y. Che, "A practical secondary frequency control strategy for virtual synchronous generator," *IEEE Trans. Smart Grid*, vol. 11, no. 3, pp. 2734–2736, May 2020.

[12] K. Shi, W. Song, H. Ge, P. Xu, Y. Yang, and F. Blaabjerg, "Transient analysis of microgrids with parallel synchronous generators and virtual synchronous generators," *IEEE Trans. Energy Convers.*, vol. 35, no. 1, pp. 95–105, Mar. 2020.

[13] V. Gevorgian, Y. Zhang, and E. Ela, "Investigating the impacts of wind generation participation in interconnection frequency response," *IEEE Trans. Sustainable Energy*, vol. 6, no. 3, pp. 1004–1012, Jul. 2015.

[14] R. K. Sarojini, K. Palanisamy, P. Sanjeevikumar, and J. B. Nielsen, "Inertia emulation control technique based frequency control of grid-connected single-phase rooftop photovoltaic system with battery and supercapacitor," *IET Renew. Power Gener.*, vol. 14, no. 7, pp. 1156–1163, May 2020.

[15] J. O'Sullivan, A. Rogers, D. Flynn, P. Smith, A. Mullane, and M. O'Malley, "Studying the maximum instantaneous non-synchronous generation in an island system—Frequency stability challenges in Ireland," *IEEE Trans. Power Syst.*, vol. 29, no. 6, pp. 2943–2951, Nov. 2014.

[16] J. Rocabert, A. Luna, F. Blaabjerg, and P. Rodríguez, "Control of power converters in AC micro-grids," *IEEE Trans. Power Electron.*, vol. 27, no. 11, pp. 4734–4749, Nov. 2012.

[17] D.-J. Kim, Y.-H. Moon, J.-J. Lee, H.-S. Ryu, and T.-H. Kim, "A new method of recording generator dynamics and its application to the derivation of synchronous machine parameters for power system stability studies," *IEEE Trans. Energy Convers.*, vol. 33, no. 2, pp. 605–616, Jun. 2018.

[18] C. Jin, W. Li, J. Shen, P. Li, L. Liu, and K. Wen, "Active frequency response based on model predictive control for bulk power system," *IEEE Trans. Power Syst.*, vol. 34, no. 4, pp. 3002–3013, Jul. 2019.

[19] C. Li, Y. Wu, Y. Sun, H. Zhang, Y. Liu, Y. Liu, and V. Terzija, "Continuous under-frequency load shedding scheme for power system adaptive frequency control," *IEEE Trans. Power Syst.*, vol. 35, no. 2, pp. 950–961, Mar. 2020.
[20] S. Wei, Y. Zhou, S. Li, and Y. Huang, "A possible configuration with motor-generator pair for renewable energy integration," *CSEE J. Power Energy Syst.*, vol. 3, no. 1, pp. 93–100, Mar. 2017.
[21] S. Wei, Y. Zhou, G. Xu, and Y. Huang, "Motor-generator pair: A novel solution to provide inertia and damping for power system with high penetration of renewable energy," *IET Gener., Transmiss. Distrib.*, vol. 11, no. 7, pp. 1839–1847, Mar. 2017.
[22] Q. Wu, Y. Huang, C. Li, Y. Gu, H. Zhao, and Y. Zhan, "Small signal stability of synchronous motor-generator pair for power system with high penetration of renewable energy," *IEEE Access*, vol. 7, pp. 166964–166974, 2019.
[23] S. Wei, Y. Zhou, and Y. Huang, "Synchronous motor-generator pair to enhance small signal and transient stability of power system with high penetration of renewable energy," *IEEE Access*, vol. 5, pp. 11505–11512, 2017.
[24] Y. Gu, Y. Huang, Q. Wu, C. Li, H. Zhao, and Y. Zhan, "Isolation and protection of the motor-generator pair system for fault ride-through of renewable energy generation systems," *IEEE Access*, vol. 8, pp. 13251–13258, 2020.
[25] *Specific Requirements for Cylindrical Rotor Synchronous Machines*, Standard GB/T 7064–2017, 2017.
[26] C. Li, Y. Huang, F. Guan, W. Fu, and Q. Wu, "Vector control strategy for motor-generator pair drive inverters in parallel operation," *IET Renew. Power Gener.*, vol. 15, no. 11, pp. 2383–2395, Apr. 2021.
[27] S. Cheng, Y. Cao, and Q. Jiang, *Theories and Methods of Power System Subsynchronous Oscillation*, Beijing, China: China Science & Publishing Media Ltd. (CSPM), 2009, pp. 129–136, ch. 4, sec. 4.
[28] P. Kundur, "Small signal stability," in *Power System Stability and Control*. New York, NY, USA: McGraw-Hill, 1994, pp. 485–508, ch. 12, sec. 4.
[29] Q. Shi, F. Li, and H. Cui, "Analytical method to aggregate multi-machine SFR model with applications in power system dynamic studies," *IEEE Trans. Power Syst.*, vol. 33, no. 6, pp. 6355–6367, Nov. 2018.
[30] P. Kundur, "Control of active power and reactive power," in *Power System Stability and Control*. New York, NY, USA: McGraw-hill, 1994, pp. 418–448, ch. 11, sec. 1.

GUOJIAN LI received the B.S. degree in electrical engineering and automation from Tianjin University, in 2003, and the M.S. degree in business administration from the Business School, China University of Political Science and Law, in 2010.

He is currently a Senior Engineer with SPIC Inner Mongolia Energy Company Ltd. He is also engaged in the production and operation of new energy enterprises and engineering construction management. His research interests include the power system operation and planning.

ERFA SHANG received the B.S. degree in power system and automation from Northeast Electric Power University, in 2002, and the M.S. degree in electrical engineering from North China Electric Power University, in 2010.

He is currently a Senior Engineer with the Inner Mongolia Xilin Gol League Dian Tou New Energy Company Ltd., and he is engaged in the management of new energy companies. His research interests include the operation and stability of new energy power grid.

QIANYU WU (Student Member, IEEE) received the Ph.D. degree in electrical engineering from North China Electric Power University (NCEPU), Beijing, China, in 2022.

She is currently working at North China Branch of State Grid Corporation of China. Her research interest includes the stability of power system with renewable energy.

CHENYANG LI (Graduate Student Member, IEEE) received the B.E. degree in electrical engineering and automation from North China Electric Power University (NCEPU), in 2014, where he is currently pursuing the Ph.D. degree with the School of Electrical and Electronic Engineering.

His research interests mainly include the stability of power system with renewable energy and power electronics.

JINPING KANG (Member, IEEE) received the B.E. degree in power system and automation from the Taiyuan University of Technology, Taiyuan, China, in 1996, and the M.E. and Ph.D. degrees in electric machines and apparatus from North China Electric Power University (NCEPU), Beijing, China, in 1999 and 2010, respectively.

She is currently an Associate Professor with the School of Electrical and Electronic Engineering, NCEPU. Her research interests include modeling of electrical machines, wireless power transfer, and data mining.